Wafer-Scale Production of Transition Metal Dichalcogenides and Alloy Monolayers by Nanocrystal Conversion for Large-Scale Ultrathin Flexible Electronics

Jihoon Kim, Hyojin Seung, Dohun Kang, Joodeok Kim, Hyeonhu Bae, Hayoung Park, Sungsu Kang, Changsoon Choi, Back Kyu Choi, Ji Soo Kim, Taeghwan Hyeon, Hoonkyung Lee, Dae-Hyeong Kim,* Sangdeok Shim,* and Jungwon Park*

Cite This: *Nano Lett.* 2021, 21, 9153–9163

Read Online

ACCESS | Metrics & More | Article Recommendations | Supporting Information

ABSTRACT: Two-dimensional (2D) transition metal dichalcogenide (TMD) layers are unit-cell thick materials with tunable physical properties according to their size, morphology, and chemical composition. Their transition of lab-scale research to industrial-scale applications requires process development for the wafer-scale growth and scalable device fabrication. Herein, we report on a new type of atmospheric pressure chemical vapor deposition (APCVD) process that utilizes colloidal nanoparticles as process-scalable precursors for the wafer-scale production of TMD monolayers. Facile uniform distribution of nanoparticle precursors on the entire substrate leads to the wafer-scale uniform synthesis of TMD monolayers with the controlled size and morphology. Composition-controlled TMD alloy monolayers with tunable bandgaps can be produced by simply mixing dual nanoparticle precursor solutions in the desired ratio. We also demonstrate the fabrication of ultrathin field-effect transistors and flexible electronics with uniformly controlled performance by using TMD monolayers.

KEYWORDS: transition metal dichalcogenides, nanoparticle precursor, wafer-scale growth, transition metal dichalcogenide alloys, ultrathin flexible electronics
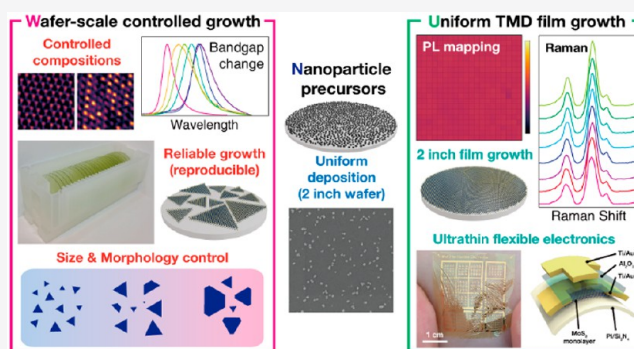
Transition metal dichalcogenide (TMD) materials with controlled compositions are attractive materials for electronics and catalysis.[1−3] This is because atom-thick TMD monolayers present unique properties in terms of exciton dynamics, the valley Hall effect, and the indirect-to-direct bandgap transition,[4−7] different from their bulk counterparts. In addition, varying the size and morphology of TMDs provides opportunities to tune the reactivity, which further enhances their potential in practical applications.[8−10] However, challenges in wafer-scale production of uniform TMD monolayers with respect to the size, morphology, and composition restrict the transformation from lab-scale research to industry-level applications in electrocatalysis, electronics, and optoelectronics.

In recent years, diverse TMD preparation methods, such as mechanical exfoliation, liquid exfoliation, and vapor−solid growth,[11−14] have been developed. Among them, chemical vapor deposition (CVD) is the most compatible method with wafer-scale processing of 2D materials. Although metal−organic CVD (MOCVD) is a typical method for the TMD growth,[15,16] it requires several hours of complicated processes

and the use of metal−organic precursors, which are toxic and expensive. Atmospheric pressure CVD (APCVD) is an attractive alternative, because it facilitates scalable TMD growth in simple and cost-effective manner.[17,18] Nevertheless, the control of size, morphology, and composition of the TMD monolayers is hampered by difficulties in the stable and ratio-controlled supply of constituent monomers by sublimation and vaporization of multiple powder precursors. Thus, the key challenge for the desired wafer-scale growth of TMD monolayers is how to achieve uniform nucleation and growth of the layers in a short time throughout the substrate by using precursors with sufficient reactivity, nontoxicity, and wafer-process compatibility.
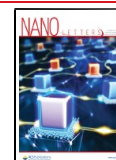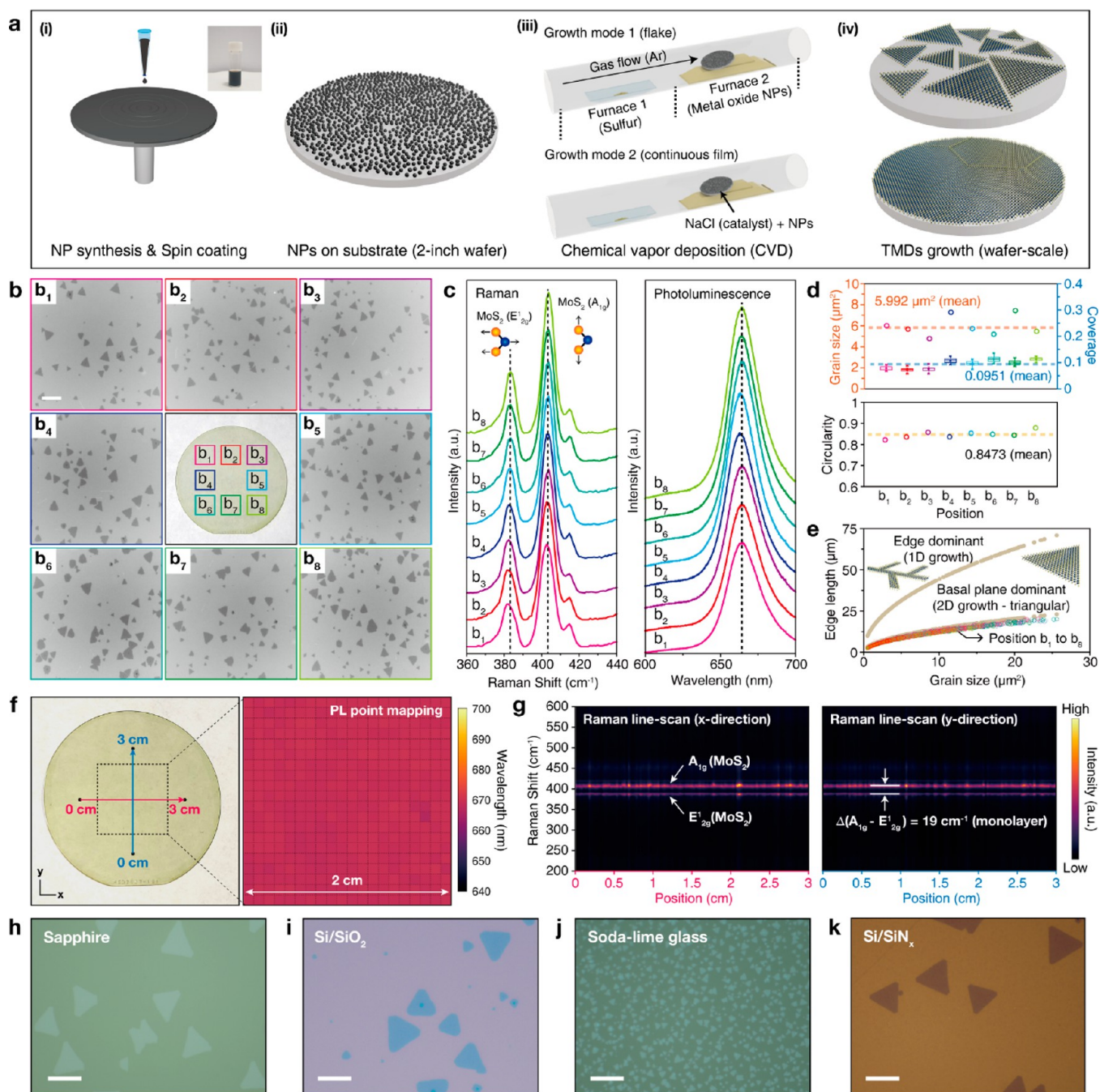
Figure 1. Uniform synthesis of MoS_2 monolayer flakes and continuous film. (a) Schematic of the entire synthetic process. (b) Photograph of a 2 in. wafer after the synthetic process and OM images of MoS_2 layers from positions b_1 to b_8 of the 2 in. wafer. Scale bar, 10 μm. (c) Raman and PL spectra of MoS_2 monolayers from positions b_1 to b_8. Dashed lines indicate the characteristic peaks of MoS_2 monolayer. (d) Averaged grain size, coverage, and circularity of thousands of MoS_2 layers from positions b_1 to b_8. (e) Plot of edge length and grain size of individual MoS_2 flakes from positions b_1 to b_8. Schematics and beige dots indicate ideal branched and triangular shapes, respectively. (f) Photograph of a 2 in. wafer covered by continuous MoS_2 film and PL spectral point mapping data of the film. (g) Raman spectra (line-scan along x (red arrow) and y (blue arrow) directions shown in part f) of the continuous film. (h−k) OM images of MoS_2 monolayer flakes grown on sapphire, Si/SiO_2, soda-lime glass, and Si/SiN_x wafers. Scale bars, 10 μm.

Herein, we develop a versatile APCVD process for wafer-scale controlled growth of TMD monolayers based on the conversion chemistry of nanoparticle precursors. Attributed to the colloidal stability and high reactivity of nanoparticles, uniform distribution of a minimum amount of precursors and homogeneous and fast growth of TMD monolayers by solid−vapor−solid transition on inch-scale substrates are accomplished. This method is readily extended to the wafer-scale

TMD alloy growth with varied compositions, such as $Mo_{1-x}W_xS_2$, with a tunable bandgap energy, simply by using mixed nanoparticle precursors. Moreover, the uniform MoS_2 film grown by our method enables the large-scale fabrication of field-effect transistors and their application to ultrathin flexible electronics with uniform performance over the entire substrate.

The overall process for the wafer-scale TMD growth is described in Figure 1a. Monodisperse transition metal oxide
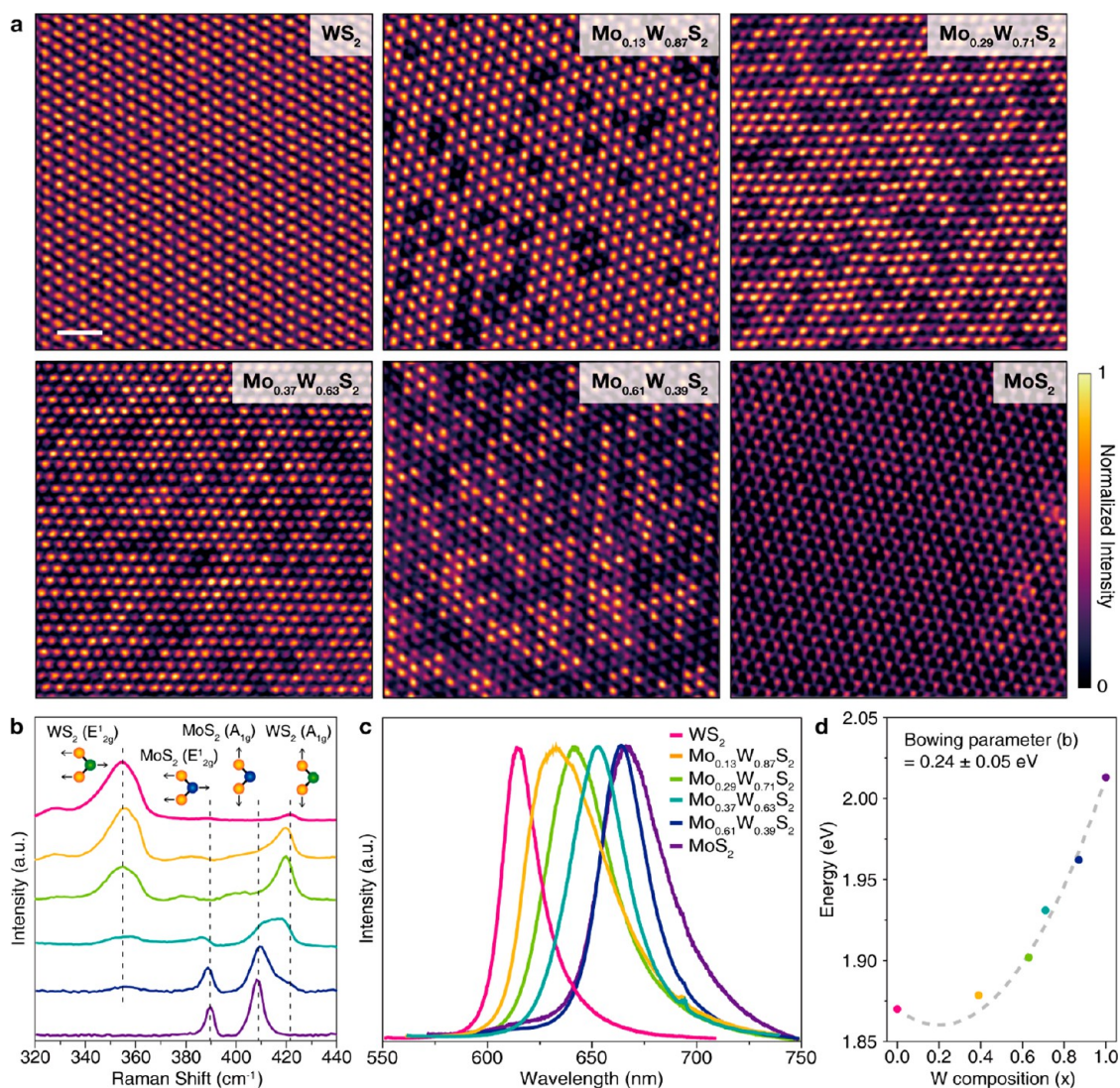
Figure 2. Synthesis and characterizations of $Mo_{1-x}W_xS_2$ alloy monolayers. (a) FFT-filtered HAADF-STEM images of $Mo_{1-x}W_xS_2$ monolayers. Scale bar, 1 nm. Intensities are normalized by MATLAB code, and images are color-mapped by normalized intensity (right, color bar). (b) Raman spectra of $Mo_{1-x}W_xS_2$ monolayers. Schematics (inset) show the vibrational modes of MoS_2 and WS_2 monolayers. Dashed lines indicate the characteristic Raman peaks of MoS_2 and WS_2 monolayers. (c) PL spectra of $Mo_{1-x}W_xS_2$ monolayers with the controlled compositions. (d) Plot of the measured optical bandgap energies of $Mo_{1-x}W_xS_2$ monolayers (x, 0−1). Calculated bowing parameter is (0.24 ± 0.05) eV.

nanoparticles, such as MoO_2 and $W_{18}O_{49}$, are prepared in a large scale by colloidal synthesis (Figure S1) and stored in a solution as precursors for TMD synthesis.[19,20] The average size of the MoO_2 nanoparticles is 56.36 nm (Figure S2). The precursors are deposited on a 2 in. wafer by spin coating, which is facilitated by the colloidal stability of the nanoparticles. To obtain the desired coverage of the nanoparticles, the concentration of the solution and the rotational speed of the spin coating are controlled (Figure S3). A uniform distribution of nanoparticles over the substrate is easily achieved without any thermal and high-vacuum systems typically used for pretreatment of the precursors, confirmed by scanning electron microscopy (SEM) (Figure S4). The substrate with the loaded nanoparticles and sulfur powder are inserted into two different furnaces in CVD for independent heating (Figure S5). The CVD process on a substrate with a tilted angle toward the direction of carrier gas (growth mode 1 in Figure 1a) provides a uniform supply of the sulfur precursor and yields TMD monolayers with controlled density.

As a representative example of growth mode 1, the wafer-scale growth of MoS_2 is demonstrated, and confirmed by the consistency in the optical microscopy (OM), Raman scattering, and photoluminescence (PL) spectra that are obtained from different positions of the substrate, marked as b_1–b_8 (Figure 1b). The Raman spectra of the layers from multiple positions of the substrate, excited by a 532 nm laser, are uniform and exhibit that the difference of two characteristic peaks (E^1_{2g} and A_{1g}) of the MoS_2 monolayer is approximately 19 cm^{-1} (Figure 1c), which is consistent with the reported value.[21] Strong and uniform peaks in the PL spectra also indicate that MoS_2 layers are monolayered and highly crystalline.[22,23] Furthermore, the projected area and perimeter of thousands of MoS_2 monolayers throughout the wafer are extracted by image processing of OM images using home-built MATLAB codes. The averaged grain size and coverage of the layers from different positions are uniform and close to 5.992 μm^2 and 0.0951, which are the mean grain size and coverage over the inch-scale wafer, respectively (Figure 1d). We also
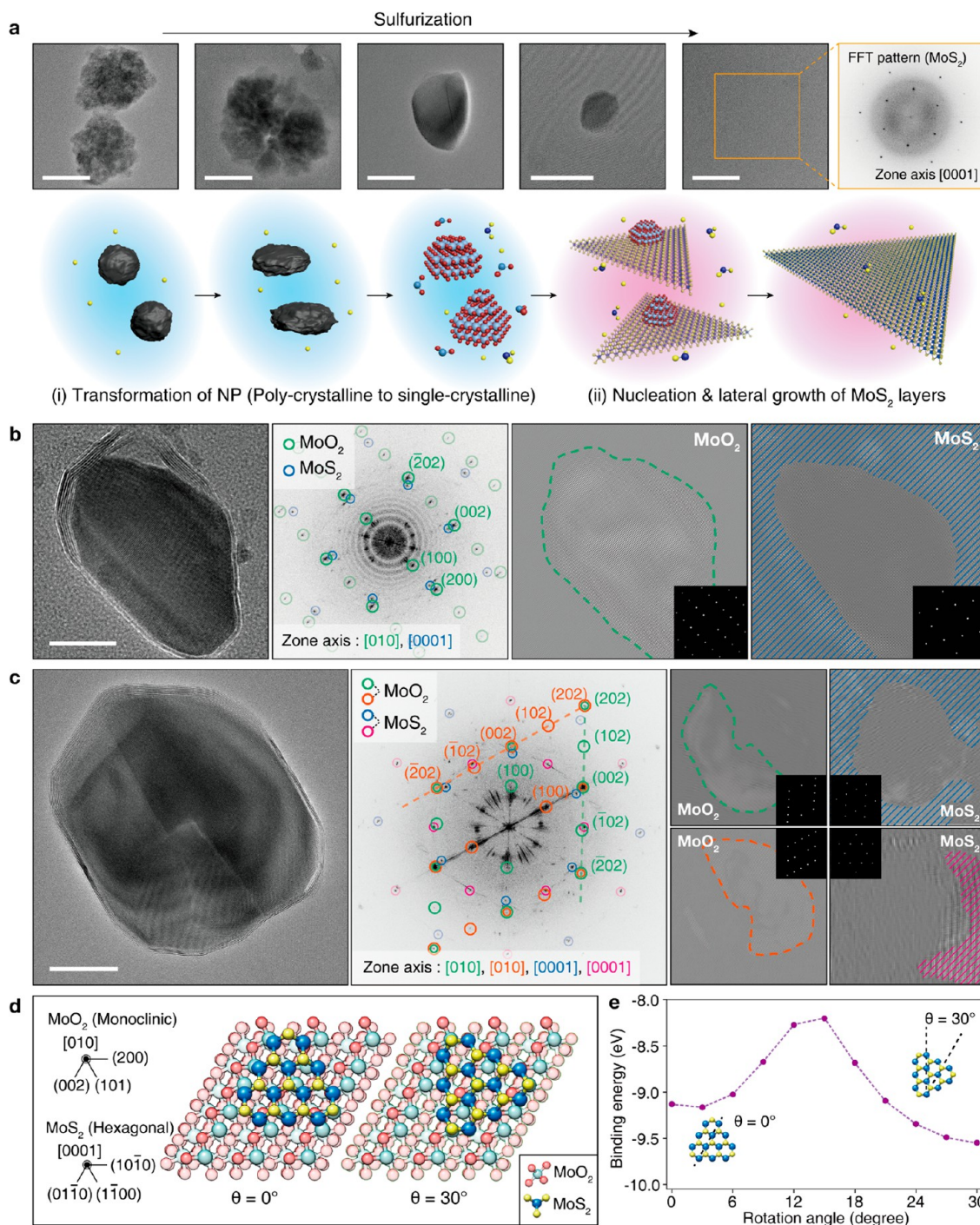
Figure 3. MoO$_2$ transformation and MoS$_2$ growth processes. (a) HRTEM images and schematics of MoO$_2$ nanoparticles and underlying grown MoS$_2$ with the progress of sulfurization. Scale bars, 50 nm. (b, c) HRTEM images, corresponding FFT patterns, and inverse FFT patterns of MoO$_2$ crystals and MoS$_2$ domains. Scale bars, 20 nm. MoO$_2$ and MoS$_2$ are marked by (green and orange) and (blue and magenta) circles, respectively. Insets are masked FFT patterns for each crystal. (d) Atomic models for MoO$_2$ and MoS$_2$ crystals arranged with rotation angles of (0 and 30)°. MoO$_2$ and MoS$_2$ domains are aligned to zone axis (Z.A.) [010] and [0001], respectively. (e) DFT calculation of binding energy between MoS$_2$ and the underlying MoO$_2$ crystals with different rotation angles.

investigate the morphological uniformity of the layers by measuring their circularity. The average circularity of the layers from different positions is close to 0.8473 (mean value). Furthermore, the plots between the grain size and the edge length measured in positions b$_1$−b$_8$ consistently follow the trend expected for the ideal triangular monolayer (Figure 1e). These results demonstrate the uniform growth of triangular monolayers throughout the substrate. To examine the epitaxial

behavior between as-grown MoS$_2$ and sapphire substrate, orientations of MoS$_2$ layers from the positions b$_1$ to b$_8$ are extracted by using MATLAB codes (Figure S6). Histograms in Figure S6 present that randomly oriented MoS$_2$ monolayers are grown in our process, although the grains aligned 30° and 90° with the [1$\bar{1}$00] direction of the sapphire substrate are dominant. This is because the sulfur precursor is moderately supplied in our growth process, and the alignment can be

further tuned by controlling the supply rate of the sulfur precursor.[24] Nanoparticle precursors mixed with NaCl (growth mode 2 in Figure 1a) promote the growth of the extended TMD film, due to the catalytic effect of sodium.[25−27] Due to the large surface-to-volume ratio and resulting high reactivity of the nanoparticles (Table S1), only 0.608 mg of MoO_2 and 0.152 μg of NaCl for MoS_2 are used for the continuous film growth on the 2 in. wafer. The uniformity of PL spectral point mapping (400 points; point interval, 1 mm) and Raman line-scan data (120 points along the x and y directions; point interval, 0.25 mm) indicates that a continuous MoS_2 monolayer film is uniformly grown over the entire substrate (Figure 1f,g). Coverage of the MoS_2 continuous film is measured by SEM, demonstrating the near full coverage throughout the entire wafer substrate (Figure S7). Merged grains in the film are coherently connected without over-lapping, confirmed by dark-field TEM imaging (Figure S8). Grain size of the film is generally 10 μm with a small population of small domains ($\sim$1 μm). Grain boundary structures are also investigated by Cs-corrected STEM analysis (Figure S9). We confirm that the merged grains are well stitched at the boundaries, regardless of their crystallographic orientations and the presence of a small portion of the incoherent boundary.[28−30] The MoS_2 growth from MoO_2 nanoparticles is also demonstrated for other types of substrates, including Si/SiO_2, soda-lime glass, and Si/SiN_x, proving the versatility of nanoparticle precursors (Figure 1h−k).

Compositional control of the TMD monolayer is a versatile method of manipulating the electronic structure and tuning the bandgap energy.[31−35] However, in the conventional CVD process, it is difficult to precisely control the stoichiometry of the TMD monolayer because the multiple powder precursors are loaded in different chambers whose thermal conditions are independently controlled, and the growth relies on their complex sublimation and transport processes. We demonstrate that our method can overcome this problem. Because the metal precursors are directly supplied on the substrate where the TMD monolayer is to grow, loading two different nanoparticle precursors facilitates improved compositional control of the TMD alloys. We synthesize $Mo_{1−x}W_xS_2$ (x, 0−1) monolayers by using a dual-precursor of molybdenum oxide and tungsten oxide nanoparticle solutions that are easily mixed and uniformly deposited on the substrate, attributing to the colloidal stability of the mixed nanoparticle precursors. Simple mixing of the dual-precursor with different concentrations (Table S2) allows the $Mo_{1−x}W_xS_2$ alloy growth with controlled compositions. High-angle annular dark-field-scanning transmission electron microscopy (HAADF-STEM) is employed to visualize the arrangement of Mo and W atoms in $Mo_{1−x}W_xS_2$ monolayers with the compositional variation, where the intensity is dependent on the atomic number[36] (Figure 2a). The ratio between W and Mo is estimated by counting the number of bright (W) and dark (Mo) atoms from multiple atomic-resolution HAADF-STEM images.

Raman spectra of the WS_2 and MoS_2 monolayers show the characteristic peaks of E^1_{2g} and A_{1g} for both materials[37−39] (Figure 2b). $Mo_{1−x}W_xS_2$ alloy monolayers show the characteristic peaks of both MoS_2 and WS_2 with changing relative intensities and peak positions between them, which correspond to the metallic composition. Most notably, PL measurements confirm that the bandgap energy is successfully tuned by the synthesis of $Mo_{1−x}W_xS_2$ alloys with the controlled composi-

tions (Figure 2c). The bandgap energies of the $Mo_{1−x}W_xS_2$ alloy monolayers match well with the bowing effect (Figure 2d), following the given eq 1:

$$E_{PL,Mo_{1−x}W_xS_2} = (1 − x)E_{PL,MoS_2} + xE_{PL,WS_2} − bx(1 − x) \tag{1}$$

where x is the tungsten (W) composition; E_{PL,MoS_2}, E_{PL,WS_2}, and $E_{PL,Mo_{1−x}W_xS_2}$ are the measured optical bandgap energies of MoS_2, WS_2, and $Mo_{1−x}W_xS_2$ monolayers, respectively; and b is the calculated bowing parameter of (0.24 ± 0.05) eV, which is the same as the reported value.[40,41] These results prove that the bandgap energy of the $Mo_{1−x}W_xS_2$ alloys is successfully tuned by the compositional change of randomly distributed atoms by using a dual-precursor.

We investigate the role of MoO_2 nanoparticle precursors for MoS_2 growth by using high-resolution transmission electron microscopy (HRTEM) of different growth stages. MoS_2 and MoO_2 nanocrystals from the different stages are transferred onto TEM grids by the surface-energy-assisted transfer method,[42] and imaged by HRTEM (Figure 3a). In the early stage of sulfurization, polycrystalline MoO_2 nanoparticles spread out and increase the size in the lateral direction of the substrate and continuously transform into nanocrystals with single or twinned domains (Figure S10a). MoS_2 monolayer is then nucleated and grows at the bottom of the MoO_2 nanoparticle that acts as a self-seeding material.[43,44] During the sulfurization, MoO_2 nanoparticles are constantly consumed by adjacently growing MoS_2 monolayers, which is indicated by the diminishing size of the particles. Cross-sectional view of the intermediate MoO_2 particles with underlying MoS_2 monolayer indicates the pancakelike morphology of the intermediate particle (Figure S10b). After exhaustion of the particle, MoS_2 monolayers are synthesized on the substrate, confirmed by fast Fourier transform (FFT).

For further understanding of how MoO_2 nanoparticles determine the growth process of MoS_2 monolayers, HRTEM images of the intermediate stages where both materials coexist are analyzed. We intentionally use an excess supply of sulfur as a means to protect and capture the intermediate MoO_2 particles by covering them with the multilayer MoS_2 shell. It facilitates further HRTEM analysis of the intermediate stages during the growth. The HRTEM image in Figure 3b shows a single-crystalline MoO_2 nanoparticle with the underlying MoS_2 monolayer. Indexing the FFT pattern based on the measured distances of lattice planes and their relative angles indicates the monoclinic MoO_2 nanocrystal aligned into the [010] zone axis (Z.A.). Interestingly, the $\{10\overline{1}0\}$ planes of the MoS_2 strongly correlate with the (002), (200), and ($\overline{2}$02) planes of monoclinic MoO_2 (green−blue paired circles). Spatial arrangement of the MoO_2 nanoparticle and the growing MoS_2 monolayer is visualized by inverse FFT obtained from independently masked FFT patterns for the two materials (inset). In addition, FIB (focused ion beam)-HRTEM analysis presents that (020) planes of the intermediate MoO_2 particle (nucleation seed) are aligned with the (0001) plane of the sapphire (Figure S11), which is consistent with Figure 3b. The MoS_2 growth from a MoO_2 nanoparticle composed of twinned domains further confirms that the growth behavior of MoS_2 is determined by the MoO_2 nanoparticle (Figure 3c). Two domains of the MoO_2 nanocrystal are independently correlated with two MoS_2 layers grown adjacently. Both domains of the twinned MoO_2 nanocrystal expose specific planes along the
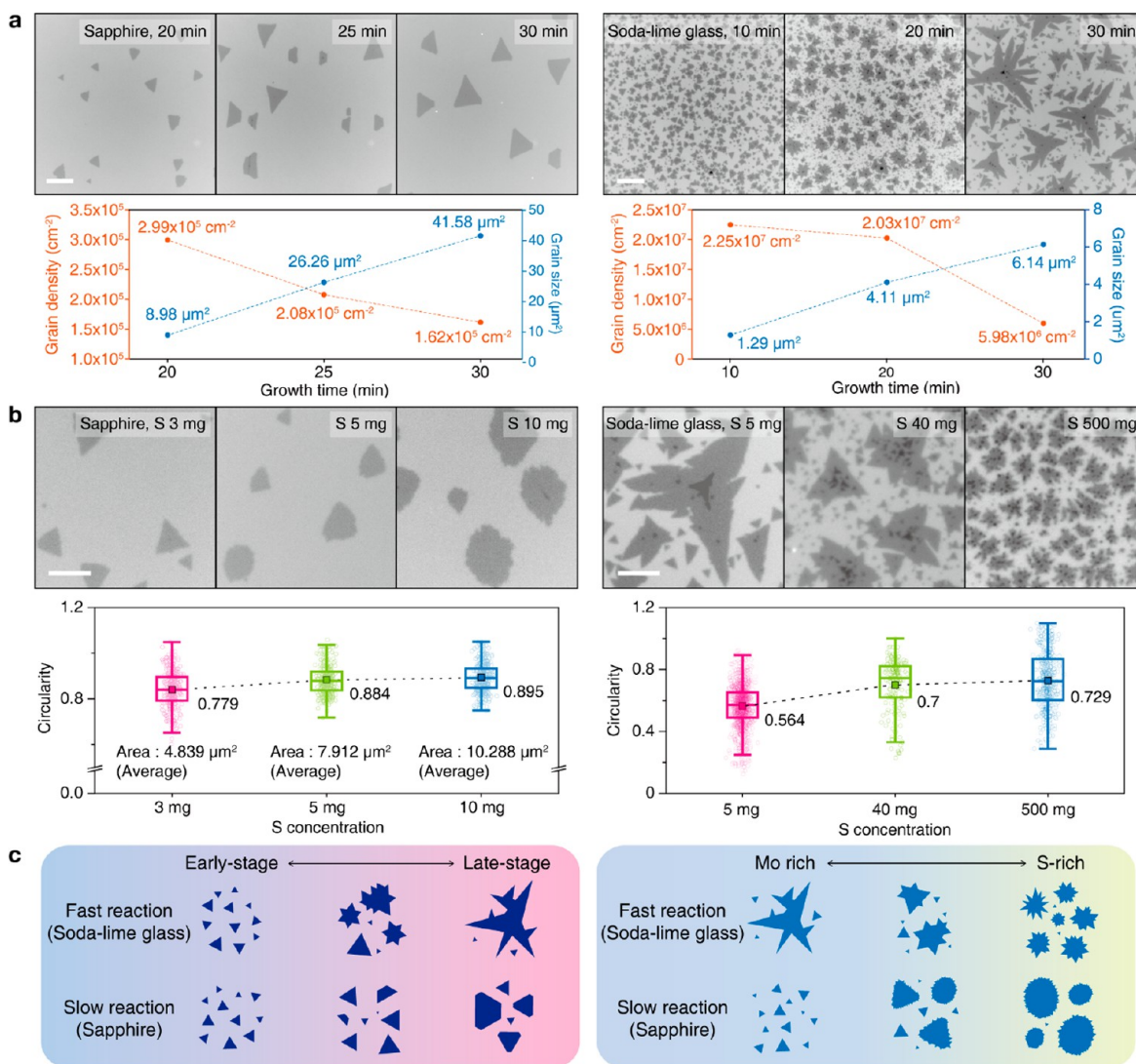
Figure 4. Controlled synthesis of MoS_2 monolayers with various growth parameters. (a) OM images of MoS_2 monolayers grown on sapphire and soda-lime glass wafer with different growth times. Plots show the change of grain density and grain size of the MoS_2 monolayer with respect to growth time. Scale bars, 10 μm. (b) OM images of MoS_2 monolayers grown on sapphire and soda-lime glass wafer with varying S concentrations. Averaged circularities of MoS_2 monolayers are shown on the plot, which indicates the change of morphology of MoS_2 layers. Scale bars, 10 μm. (c) Schematic illustrations of the size and shape evolution of MoS_2 monolayers by changing the growth parameters with different kinetic controls.

Z.A. [010] (Figure S12). The (002), (200), and ($\bar{2}$02) planes of one MoO_2 domain with the Z.A. [010] are associated with the orientation of the underlying MoS_2 monolayer in a consistent way, as observed in Figure 3b (green−blue paired circles). The orientation of the MoS_2 monolayer from another twinned MoO_2 domain with the Z.A. [010] rotated by 30° (orange−magenta paired circles). Inverse FFT patterns of the two domains of MoO_2 and the independently grown MoS_2 monolayers represent their arrangements. Furthermore, density functional theory (DFT) calculation reveals energetically preferred orientations in the growth of MoS_2 {10$\bar{1}$0} on MoO_2 (200) (Figure 3d,e). A local minima of the binding energy are observed at around (0 and 30)° rotation angles, which is consistent with the experimental data.

The functionality of the TMD monolayer in various applications can be improved by controlling the size and morphology.[45−47] We demonstrate that the size and shape of MoS_2 monolayers can be easily tuned by manipulating the growth parameters, confirmed by quantitative analysis of MoS_2

layers from different parameters that include the growth time, precursor concentration, and substrate type. With prolonged growth time, MoS_2 on sapphire increases the average grain size while maintaining triangular morphologies with marginal truncation of corners, and the proportion of small grains is gradually reduced, as indicated by the OM images and plots in Figure 4a. The MoS_2 growth on soda-lime glass is initiated by densely packed nucleation sites, possibly due to the catalytic characteristic of the substrate.[27] The growth results in multiple-branched morphology with the increased size, as it is highly kinetically controlled (Figure 4a). In both cases, ripening of preformed domains occurs in the late stage of sulfurization, since the monomer concentration is locally limited, which allows the consumption of unstable small grains by adjacently growing monolayers. Furthermore, the ratio of molybdenum to sulfur manipulates the edge structure of the layer, resulting in different morphologies. The shape evolution associated with the sulfur concentration is investigated with OM images and circularity. The OM images and measured
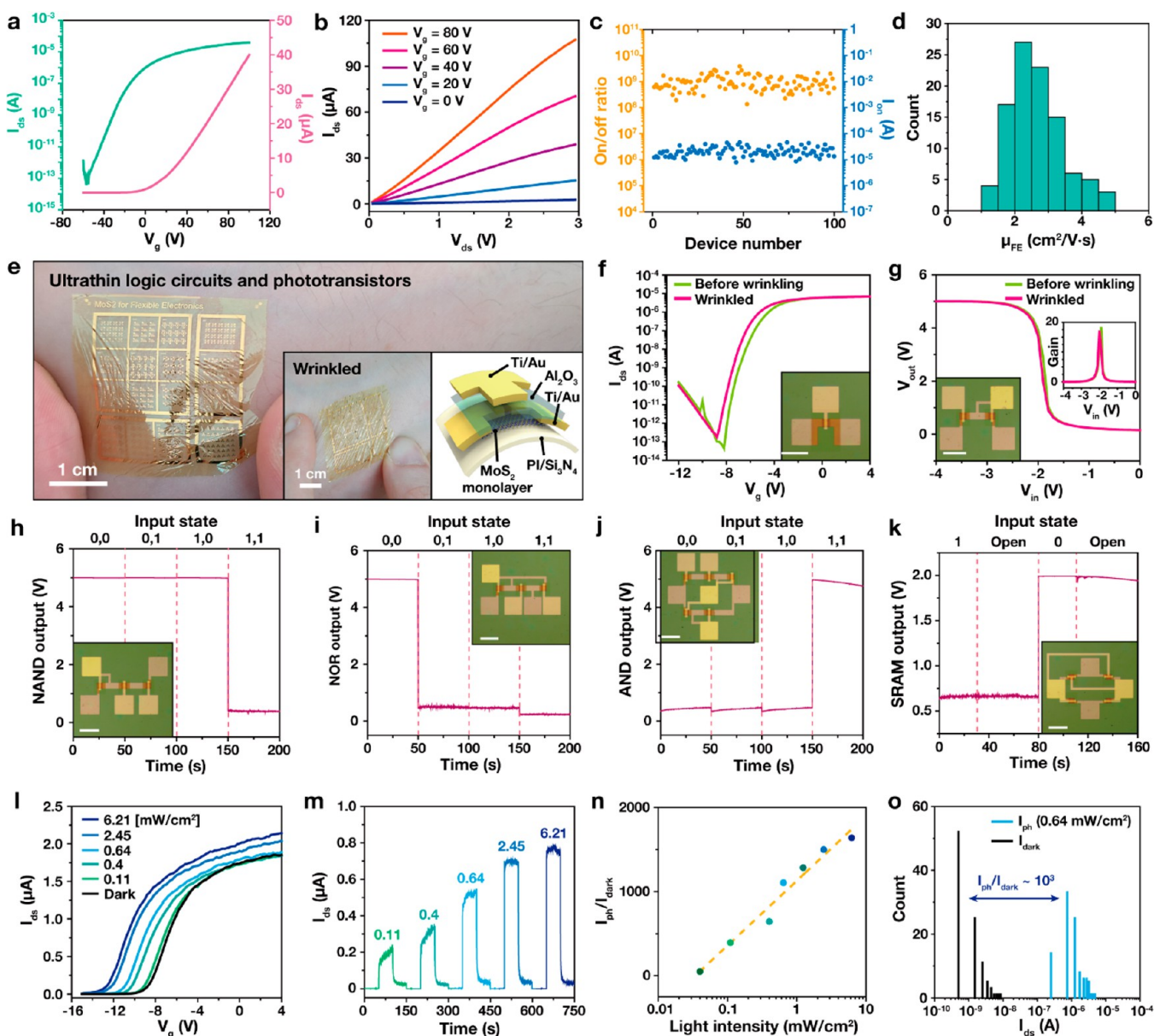
Figure 5. Characterization of MoS_2 transistors, ultrathin logic circuits, and phototransistors. (a) Transfer curves at V_{ds} = 1 V. (b) Output characteristics. (c, d) The distribution of on/off ratio, on-current (c, left and right axis), and field-effect mobility (d) measurements from 100 random devices. (e) Photograph of the ultrathin logic circuits and phototransistors attached on human skin. The left inset shows a photograph of the ultrathin device wrinkled on human skin. The right inset shows a schematic of ultrathin MoS_2 FETs. (f, g) Transfer curves of the ultrathin MoS_2 FET (f) and inverter (g) before wrinkling (green) and after wrinkling (pink). V_{dd} = 5 V. Inset shows the voltage gain. Scale bars (inset), 200 μm. (h−k) Output characteristics of NAND (h), NOR (i), and AND gates (j) at V_{dd} = 5 V and SRAM (k) at V_{dd} = 2 V. Scale bars (Inset), 200 μm. (l) Transfer curves under the dark and different light intensities (532 nm). (m) Time-resolved photocurrents under different light intensities at V_{ds} = 1 V and V_g = −10 V. (n) The ratio of photocurrent to dark current under different light intensities. (o) The distribution of dark current and photocurrent under A light intensity of 0.64 mW/cm^2 measured from a 10 × 10 phototransistor array.

circularities, shown in Figure 4b, show that in high sulfur concentrations, sharp triangular layers become round-shaped layers with rough edge interfaces. The effect of the ratio of the two precursors is more obvious in the MoS_2 growth on soda-lime glass. The molybdenum-dominant environment induced by the limited sulfur supply promotes the growth of layers with sharp edges, indicated by the low circularity (0.564). In contrast, with an excess of sulfur, MoS_2 monolayers show highly dendritic morphologies with relatively homogeneous size distribution, presumably by suppression of the ripening process.[48,49] The schematics of Figure 4c summarize the size

and shape evolution process of the MoS_2 monolayer on different substrates.

The uniform wafer-scale synthesis of the MoS_2 film offers great potential for high-performance electronic and optoelectronic devices, including flexible electronics.[50,51] To demonstrate such potential, the as-grown MoS_2 film is transfer-printed from a sapphire wafer to various desired substrates (e.g., silicon oxide wafer, flexible polyimide substrate), and various devices are fabricated. For the transfer printing, our modified transfer method is applied,[42] facilitating the intact transfer of the MoS_2 film onto the desired substrate without any noticeable wrinkles (Figure S13).

In order to investigate the uniformity of the MoS_2 film, we fabricate a batch of MoS_2 field-effect transistors (FETs) (3078 transistors shown in Figure S14a). The MoS_2 FET has a bottom-gate structure (Figure S14b). A brief description of the fabrication procedure is as follows. First, the MoS_2 film is transferred onto a 2 in. SiO_2/Si wafer (300 nm thick SiO_2 layer on a Si wafer). Then, the film is patterned by photolithography and dry etching. Afterward, Ti/Au layers (5 nm/25 nm) are deposited by thermal evaporation and patterned by the lift-off process to form source/drain electrodes. Finally, Al_2O_3 is deposited by the atomic layer deposition (ALD) process to form a passivation layer (20 nm). Transfer curves ($I_{ds}-V_g$) and output current characteristics ($I_{ds}-V_{ds}$) of a representative transistor (channel length and width, 5 and 60 μm) are shown in Figure 5a,b. The key device features include the field-effect mobility (μ_{FE}) of 4.13 cm^2/V s, off-current (I_{off}) of 37 fA, on-current (I_{on}) of 39.9 μA, and an on/off ratio of 10^9. The device characterization data, such as I_{on}, I_{off}, on/off ratio, μ_{FE}, and threshold voltage (V_{TH}), are collected from 100 randomly selected transistors. The transfer curves of the transistors are shown in Figure S14c,d. Figure 5c shows the on/off ratio (left axis) and I_{on} (right axis) with a mean value of 10^9 and 21.9 μA, respectively. Figure 5d shows the μ_{FE} data, whose average, standard deviation, and maximum are 2.64 cm^2/V s, 0.8 cm^2/V s, and 5 cm^2/V s, respectively. The threshold voltages are mostly in the range of 0−5 V (Figure S14e).

Based on the uniform MoS_2 FETs, we fabricate an ultrathin flexible type of logic circuit (e.g., inverter, NAND gate, NOR gate, AND gate, and SRAM) and phototransistors. Due to their ultrathin flexible nature, the devices have the potential for skin-mounted electronics (Figure 5e). Detailed layouts of the circuits and phototransistor are shown in Figure S15. As illustrated in Figure 5e (right inset), the ultrathin MoS_2 FET has a top-gate structure that consists of polyimide/silicon nitride (PI/Si_3N_4) substrate (420 nm/25 nm), MoS_2 monolayer channel, Ti/Au source/drain electrodes (5 nm/25 nm), Al_2O_3 dielectric layer (25 nm), Ti/Au gate (5 nm/25 nm), and parylene film for the top encapsulation (500 nm). Due to the intrinsic softness of the MoS_2 film and the ultrathin device thickness (∼1 μm), the devices are tolerable against external mechanical deformations (Figure 5e, left inset). For example, the transfer characteristics show minimal changes under its mechanical deformation (Figure 5f). A transfer curve ($V_{in}-V_{out}$) of the inverter is shown in Figure 5g. The inverter shows a voltage gain of 18.5 at V_{dd} = 5 V, and stable operation, even under its wrinkled state. Other types of logic gates are also fabricated by using the ultrathin FETs and inverters as building blocks (Figure S16). The NAND gate and NOR gate consist of a transistor and an inverter (Figure 5h,i). The AND gate is the combination of a NAND gate and an inverter (Figure 5j). These logic gates exhibit the output logic state of either "0" (0 V) or "1" (5 V), according to four states of two inputs (e.g., (0,0), (0,1), (1,0), and (1,1)) with V_{dd} = 5 V. SRAM, which is a flip−flop memory cell, consists of two cross-coupled inverters (Figure 5k). When the input is set to "1" at 0 s or "0" at 80 s, the logic state becomes "0" or "1", respectively. The logic state can be maintained for 50 s, even after the input is opened at 30 or 110 s, exhibiting stable memory performance. The reliable operation of logic gates corroborates the potential of the MoS_2 film for applications to large-scale integrated circuits.

Besides applications to flexible electronics, MoS_2 can be applied to flexible optoelectronics, such as photodetectors, by utilizing its high photoabsorption coefficient.[52,53] A 10 × 10 array of ultrathin phototransistors is fabricated (Figure S17a). The transfer curves ($I_{ds}-V_g$) of a representative photo-transistor illuminated by 532 nm light is shown in Figure 5l. The time-resolved photocurrent responses are measured at V_g = −10 V by gradually increasing light intensities, showing light-sensitive current responses (Figure 5m). Typically, the MoS_2 phototransistor features residual photoconductivity due to charge trapping, even after the light illumination is removed.[54] Therefore, trapped charges are released every 150 s by applying a positive gate bias to maintain a low level of dark current (∼1 nA). The ratio of photocurrent (I_{ph}) to dark current (I_{dark}) is proportional to the intensity of the illuminated light (Figure 5n). The photoresponsivity is 556 A/W at a light intensity of 0.11 mW/cm^2 (Figure S17b). I_{dark} and I_{ph} of 100 devices in the array are measured under a light intensity of 0.64 mW/cm^2 (Figure 5o), whose mean values are 1.52 nA and 1.31 μA, respectively, and thus I_{ph}/I_{dark} is ∼10^3.

We develop a wafer-scale controlled synthetic process of TMD monolayers, which utilizes transition metal oxide nanoparticles as precursors. Facile deposition of precursors with uniform coverage on the inch-scale substrate facilitates the reproducible and massive production of TMD monolayers. The use of different mixing ratios of the dual-precursor, such as MoO_2 and $W_{18}O_{49}$ nanoparticles, enables one to manipulate the composition of the $Mo_{1-x}W_xS_2$ alloys, which allows the wafer-scale production of 2D materials with a tunable optical bandgap. Furthermore, our method can be widely applied to the mass production of various 2D materials, with controllability in terms of the coverage, morphology, and doping level. Ultrathin field-effect transistors and flexible electronic devices with uniform performance are fabricated by utilizing the continuous MoS_2 film, which demonstrates versatile device applications of TMD monolayers obtained from the new synthetic process.

■ ASSOCIATED CONTENT

ⓢ Supporting Information

The Supporting Information is available free of charge at https://pubs.acs.org/doi/10.1021/acs.nanolett.1c02991.

Experimental section and supporting data such as TMD growth, characterization, DFT calculation, and device fabrication (PDF)

■ AUTHOR INFORMATION

Corresponding Authors

Jungwon Park − *Center for Nanoparticle Research, Institute for Basic Science (IBS), Seoul 08826, Republic of Korea; School of Chemical and Biological Engineering, Institute of Chemical Process, Seoul National University, Seoul 08826, Republic of Korea; Institute of Engineering Research, Seoul National University, Seoul 08826, Republic of Korea;* ⓞ orcid.org/0000-0003-2927-4331; Email: jungwonpark@snu.ac.kr

Sangdeok Shim − *Department of Chemistry, Sunchon National University, Sunchon 57922, Republic of Korea;* ⓞ orcid.org/0000-0001-5887-565X; Email: san90@scnu.ac.kr

Dae-Hyeong Kim − *Center for Nanoparticle Research, Institute for Basic Science (IBS), Seoul 08826, Republic of Korea; School of Chemical and Biological Engineering, Institute of Chemical Process, Seoul National University,*

Seoul 08826, Republic of Korea; Department of Materials Science and Engineering, Seoul National University, Seoul 08826, Republic of Korea; ◉ orcid.org/0000-0002-4722-1893; Email: dkim98@snu.ac.kr

Authors

Jihoon Kim − *Center for Nanoparticle Research, Institute for Basic Science (IBS), Seoul 08826, Republic of Korea; School of Chemical and Biological Engineering, Institute of Chemical Process, Seoul National University, Seoul 08826, Republic of Korea;* ◉ orcid.org/0000-0003-2760-2610

Hyojin Seung − *Center for Nanoparticle Research, Institute for Basic Science (IBS), Seoul 08826, Republic of Korea; School of Chemical and Biological Engineering, Institute of Chemical Process, Seoul National University, Seoul 08826, Republic of Korea*

Dohun Kang − *Center for Nanoparticle Research, Institute for Basic Science (IBS), Seoul 08826, Republic of Korea; School of Chemical and Biological Engineering, Institute of Chemical Process, Seoul National University, Seoul 08826, Republic of Korea;* ◉ orcid.org/0000-0001-5965-6432

Joodeok Kim − *Center for Nanoparticle Research, Institute for Basic Science (IBS), Seoul 08826, Republic of Korea; School of Chemical and Biological Engineering, Institute of Chemical Process, Seoul National University, Seoul 08826, Republic of Korea*

Hyeonhu Bae − *Department of Physics, Konkuk University, Seoul 05029, Republic of Korea;* ◉ orcid.org/0000-0001-7276-6636

Hayoung Park − *Center for Nanoparticle Research, Institute for Basic Science (IBS), Seoul 08826, Republic of Korea; School of Chemical and Biological Engineering, Institute of Chemical Process, Seoul National University, Seoul 08826, Republic of Korea*

Sungsu Kang − *Center for Nanoparticle Research, Institute for Basic Science (IBS), Seoul 08826, Republic of Korea; School of Chemical and Biological Engineering, Institute of Chemical Process, Seoul National University, Seoul 08826, Republic of Korea*

Changsoon Choi − *Center for Nanoparticle Research, Institute for Basic Science (IBS), Seoul 08826, Republic of Korea; School of Chemical and Biological Engineering, Institute of Chemical Process, Seoul National University, Seoul 08826, Republic of Korea*

Back Kyu Choi − *Center for Nanoparticle Research, Institute for Basic Science (IBS), Seoul 08826, Republic of Korea; School of Chemical and Biological Engineering, Institute of Chemical Process, Seoul National University, Seoul 08826, Republic of Korea*

Ji Soo Kim − *Center for Nanoparticle Research, Institute for Basic Science (IBS), Seoul 08826, Republic of Korea; School of Chemical and Biological Engineering, Institute of Chemical Process, Seoul National University, Seoul 08826, Republic of Korea*

Taeghwan Hyeon − *Center for Nanoparticle Research, Institute for Basic Science (IBS), Seoul 08826, Republic of Korea; School of Chemical and Biological Engineering, Institute of Chemical Process, Seoul National University, Seoul 08826, Republic of Korea;* ◉ orcid.org/0000-0001-5959-6257

Hoonkyung Lee − *Department of Physics, Konkuk University, Seoul 05029, Republic of Korea;* ◉ orcid.org/0000-0002-6417-1648

Complete contact information is available at:
https://pubs.acs.org/10.1021/acs.nanolett.1c02991

Author Contributions

J.K. (Jihoon Kim) and J.P. planned the research. J.K. (Jihoon Kim), H.S., S.K., B.K.C., J.S.K., T.H., S.S., and J.P. discussed and/or acquired the data. H.S., C.C., and D.-H.K. fabricated the ultrathin flexible electronics and transistors. D.K., H.B., and H.L. performed the DFT calculation. J.K. (Jihoon Kim), J.K. (Joodeok Kim), and H.P. conducted the image processing. J.K. (Jihoon Kim), H.S., D.-H.K., and J.P. wrote the manuscript. D.-H.K., S.S., and J.P. supervised the research. All authors contributed to the discussion of results.

Notes

The authors declare no competing financial interest.

■ REFERENCES

(1) Radisavljevic, B.; Radenovic, A.; Brivio, J.; Giacometti, V.; Kis, A. Single-layer MoS$_2$ Transistors. *Nat. Nanotechnol.* **2011**, *6*, 147−150.

(2) Shi, W.; Kahn, S.; Jiang, L.; Wang, S.-Y.; Tsai, H.-Z.; Wong, D.; Taniguchi, T.; Watanabe, K.; Wang, F.; Crommie, M. F.; Zettl, A. Reversible Writing of High-Mobility and High-Carrier-Density Doping Patterns in Two-Dimensional van der Waals Heterostructures. *Nat. Electron.* **2020**, *3*, 99−105.

(3) Karunadasa, H. I.; Montalvo, E.; Sun, Y.; Majda, M.; Long, J. R.; Chang, C. J. A Molecular MoS$_2$ Edge Site Mimic for Catalytic Hydrogen Generation. *Science* **2012**, *335*, 698−702.

(4) Jin, C.; Regan, E. C.; Wang, D.; Iqbal Bakti Utama, M.; Yang, C.-S.; Cain, J.; Qin, Y.; Shen, Y.; Zheng, Z.; Watanabe, K.; Taniguchi, T.; Tongay, S.; Zettl, A.; Wang, F. Identification of Spin, Valley and Moiré Quasi-Angular Momentum of Interlayer Excitons. *Nat. Phys.* **2019**, *15*, 1140−1144.

(5) Nayak, P. K.; Horbatenko, Y.; Ahn, S.; Kim, G.; Lee, J.-U.; Ma, K. Y.; Jang, A.-R.; Lim, H.; Kim, D.; Ryu, S.; Cheong, H.; Park, N.; Shin, H. S. Probing Evolution of Twist-Angle-Dependent Interlayer Excitons in MoSe$_2$/WSe$_2$ van der Waals Heterostructures. *ACS Nano* **2017**, *11*, 4041−4050.

(6) Mak, K. F.; McGill, K. L.; Park, J.; McEuen, P. L. The Valley Hall Effect in MoS$_2$ Transistors. *Science* **2014**, *344*, 1489−1492.

(7) Mak, K. F.; Lee, C.; Hone, J.; Shan, J.; Heinz, T. F. Atomically Thin MoS$_2$: A New Direct-Gap Semiconductor. *Phys. Rev. Lett.* **2010**, *105*, 136805.

(8) Yin, X.; Ye, Z.; Chenet, D. A.; Ye, Y.; O'Brien, K.; Hone, J. C.; Zhang, X. Edge Nonlinear Optics on a MoS$_2$ Atomic Monolayer. *Science* **2014**, *344*, 488−490.

(9) Voiry, D.; Fullon, R.; Yang, J.; de Carvalho Castro e Silva, C.; Kappera, R.; Bozkurt, I.; Kaplan, D.; Lagos, M. J.; Batson, P. E.; Gupta, G.; Mohite, A. D.; Dong, L.; Er, D.; Shenoy, V. B.; Asefa, T.; Chhowalla, M. The Role of Electronic Coupling between Substrate and 2D MoS_2 Nanosheets in Electrocatalytic Production of Hydrogen. *Nat. Mater.* **2016**, *15*, 1003−1009.

(10) Zhang, J.; Yu, H.; Chen, W.; Tian, X.; Liu, D.; Cheng, M.; Xie, G.; Yang, W.; Yang, R.; Bai, X.; Shi, D.; Zhang, G. Scalable Growth of High-Quality Polycrystalline MoS_2 Monolayers on SiO_2 with Tunable Grain Sizes. *ACS Nano* **2014**, *8*, 6024−6030.

(11) Shim, J.; Bae, S.-H.; Kong, W.; Lee, D.; Qiao, K.; Nezich, D.; Park, Y. J.; Zhao, R.; Sundaram, S.; Li, X.; Yeon, H.; Choi, C.; Kum, H.; Yue, R.; Zhou, G.; Ou, Y.; Lee, K.; Moodera, J.; Zhao, X.; Ahn, J.-H.; Hinkle, C.; Ougazzaden, A.; Kim, J. Controlled Crack Propagation for Atomic Precision Handling of Wafer-Scale Two-Dimensional Materials. *Science* **2018**, *362*, 665−670.

(12) Yin, Z.; Li, H.; Li, H.; Jiang, L.; Shi, Y.; Sun, Y.; Lu, G.; Zhang, Q.; Chen, X.; Zhang, H. Single-Layer MoS_2 Phototransistors. *ACS Nano* **2012**, *6*, 74−80.

(13) Coleman, J. N.; Lotya, M.; O'Neill, A.; Bergin, S. D.; King, P. J.; Khan, U.; Young, K.; Gaucher, A.; De, S.; Smith, R. J.; Shvets, I. V.; Arora, S. K.; Stanton, G.; Kim, H.-Y.; Lee, K.; Kim, G. T.; Duesberg, G. S.; Hallam, T.; Boland, J. J.; Wang, J. J.; Donegan, J. F.; Grunlan, J. C.; Moriarty, G.; Shmeliov, A.; Nicholls, R. J.; Perkins, J. M.; Grieveson, E. M.; Theuwissen, K.; McComb, D. W.; Nellist, P. D.; Nicolosi, V. Two-Dimensional Nanosheets Produced by Liquid Exfoliation of Layered Materials. *Science* **2011**, *331*, 568−571.

(14) van der Zande, A. M.; Huang, P. Y.; Chenet, D. A.; Berkelbach, T. C.; You, Y.; Lee, G.-H.; Heinz, T. F.; Reichman, D. R.; Muller, D. A.; Hone, J. C. Grains and Grain Boundaries in Highly Crystalline Monolayer Molybdenum Disulphide. *Nat. Mater.* **2013**, *12*, 554−561.

(15) Kang, K.; Xie, S.; Huang, L.; Han, Y.; Huang, P. Y.; Mak, K. F.; Kim, C.-J.; Muller, D.; Park, J. High-Mobility Three-Atom-Thick Semiconducting Films with Wafer-Scale Homogeneity. *Nature* **2015**, *520*, 656−660.

(16) Cohen, A.; Patsha, A.; Mohapatra, P. K.; Kazes, M.; Ranganathan, K.; Houben, L.; Oron, D.; Ismach, A. Growth-Etch Metal-Organic Chemical Vapor Deposition Approach of WS_2 Atomic Layers. *ACS Nano* **2021**, *15*, 526−538.

(17) Wang, J.; Cai, X.; Shi, R.; Wu, Z.; Wang, W.; Long, G.; Tang, Y.; Cai, N.; Ouyang, W.; Geng, P.; Chandrashekar, B. N.; Amini, A.; Wang, N.; Cheng, C. Twin Defect Derived Growth of Atomically Thin MoS_2 Dendrites. *ACS Nano* **2018**, *12*, 635−643.

(18) Xu, Z.-Q.; Zhang, Y.; Lin, S.; Zheng, C.; Zhong, Y. L.; Xia, X.; Li, Z.; Sophia, P. J.; Fuhrer, M. S.; Cheng, Y.-B.; Bao, Q. Synthesis and Transfer of Large-Area Monolayer WS_2 Crystals: Moving Toward the Recyclable Use of Sapphire Substrates. *ACS Nano* **2015**, *9*, 6178−6187.

(19) Dou, J.; Zeng, H. C. Targeted Synthesis of Silicomolybdic Acid (Keggin Acid) inside Mesoporous Silica Hollow Spheres for Friedel−Crafts Alkylation. *J. Am. Chem. Soc.* **2012**, *134*, 16235−16246.

(20) Qiu, J.; Xiao, Q.; Zheng, X.; Zhang, L.; Xing, H.; Ni, D.; Liu, Y.; Zhang, S.; Ren, Q.; Hua, Y.; Zhao, K.; Bu, W. Single $W_{18}O_{49}$ Nanowires: A Multifunctional Nanoplatform for Computed Tomography Imaging and Photothermal/Photodynamic/Radiation Synergistic Cancer Therapy. *Nano Res.* **2015**, *8*, 3580−3590.

(21) Li, H.; Zhang, Q.; Yap, C. C. R.; Tay, B. K.; Edwin, T. H. T.; Olivier, A.; Baillargeat, D. From Bulk to Monolayer MoS_2: Evolution of Raman Scattering. *Adv. Funct. Mater.* **2012**, *22*, 1385−1390.

(22) Splendiani, A.; Sun, L.; Zhang, Y.; Li, T.; Kim, J.; Chim, C.-Y.; Galli, G.; Wang, F. Emerging Photoluminescence in Monolayer MoS_2. *Nano Lett.* **2010**, *10*, 1271−1275.

(23) Ji, Q.; Zhang, Y.; Gao, T.; Zhang, Y.; Ma, D.; Liu, M.; Chen, Y.; Qiao, X.; Tan, P.-H.; Kan, M.; Feng, J.; Sun, Q.; Liu, Z. Epitaxial Monolayer MoS_2 on Mica with Novel Photoluminescence. *Nano Lett.* **2013**, *13*, 3870−3877.

(24) Suenaga, K.; Ji, H. G.; Lin, Y.-C.; Vincent, T.; Maruyama, M.; Aji, A. S.; Shiratsuchi, Y.; Ding, D.; Kawahara, K.; Okada, S.; Panchal, V.; Kazakova, O.; Hibino, H.; Suenaga, K.; Ago, H. Surface-Mediated Aligned Growth of Monolayer MoS_2 and In-Plane Heterostructures with Graphene on Sapphire. *ACS Nano* **2018**, *12* (10), 10032−10044.

(25) Li, S.; Lin, Y.-C.; Zhao, W.; Wu, J.; Wang, Z.; Hu, Z.; Shen, Y.; Tang, D.-M.; Wang, J.; Zhang, Q.; Zhu, H.; Chu, L.; Zhao, W.; Liu, C.; Sun, Z.; Taniguchi, T.; Osada, M.; Chen, W.; Xu, Q.-H.; Wee, A. T. S.; Suenaga, K.; Ding, F.; Eda, G. Vapour-Liquid-Solid Growth of Monolayer MoS_2 Nanoribbons. *Nat. Mater.* **2018**, *17*, 535−542.

(26) Li, J.; Yan, W.; Lv, Y.; Leng, J.; Zhang, D.; ÓCoileáin, C.; Cullen, C. P.; Stimpel-Lindner, T.; Duesberg, G. S.; Cho, J.; Choi, M.; Chun, B. S.; Zhao, Y.; Lv, C.; Arora, S. K.; Wu, H.-C. Sub-Millimeter Size High Mobility Single Crystal $MoSe_2$ Monolayers Synthesized by NaCl-assisted Chemical Vapor Deposition. *RSC Adv.* **2020**, *10*, 1580−1587.

(27) Yang, P.; Zou, X.; Zhang, Z.; Hong, M.; Shi, J.; Chen, S.; Shu, J.; Zhao, L.; Jiang, S.; Zhou, X.; Huan, Y.; Xie, C.; Gao, P.; Chen, Q.; Zhang, Q.; Liu, Z.; Zhang, Y. Batch Production of 6-Inch Uniform Monolayer Molybdenum Disulfide Catalyzed by Sodium in Glass. *Nat. Commun.* **2018**, *9*, 979.

(28) Zhou, W.; Zou, X.; Najmaei, S.; Liu, Z.; Shi, Y.; Kong, J.; Lou, J.; Ajayan, P. M.; Yakobson, B. I.; Idrobo, J.-C. Intrinsic Structural Defects in Monolayer Molybdenum Disulfide. *Nano Lett.* **2013**, *13* (6), 2615−2622.

(29) Zhou, S.; Wang, S.; Shi, Z.; Sawada, H.; Kirkland, A. I.; Li, J.; Warner, J. H. Atomically Sharp Interlayer Stacking Shifts at Antiphase Grain Boundaries in Overlapping MoS_2 Secondary Layers. *Nanoscale* **2018**, *10*, 16692−16702.

(30) Ly, T. H.; Perello, D. J.; Zhao, J.; Deng, Q.; Kim, H.; Han, G. H.; Chae, S. H.; Jeong, H. Y.; Lee, Y. H. Misorientation-Angle-Dependent Electrical Transport across Molybdenum Disulfide Grain Boundaries. *Nat. Commun.* **2016**, *7*, 10426.

(31) Zhou, J.; Lin, J.; Huang, X.; Zhou, Y.; Chen, Y.; Xia, J.; Wang, H.; Xie, Y.; Yu, H.; Lei, J.; Wu, D.; Liu, F.; Fu, Q.; Zeng, Q.; Hsu, C.-H.; Yang, C.; Lu, L.; Yu, T.; Shen, Z.; Lin, H.; Yakobson, B. I.; Liu, Q.; Suenaga, K.; Liu, G.; Liu, Z. A Library of Atomically Thin Metal Chalcogenides. *Nature* **2018**, *556*, 355−359.

(32) Susarla, S.; Kutana, A.; Hachtel, J. A.; Kochat, V.; Apte, A.; Vajtai, R.; Idrobo, J. C.; Yakobson, B. I.; Tiwary, C. S.; Ajayan, P. M. Quaternary 2D Transition Metal Dichalcogenides (TMDs) with Tunable Bandgap. *Adv. Mater.* **2017**, *29*, 1702457.

(33) Duan, X.; Wang, C.; Fan, Z.; Hao, G.; Kou, L.; Halim, U.; Li, H.; Wu, X.; Wang, Y.; Jiang, J.; Pan, A.; Huang, Y.; Yu, R.; Duan, X. Synthesis of $WS_{2x}Se_{2−2x}$ Alloy Nanosheets with Composition-Tunable Electronic Properties. *Nano Lett.* **2016**, *16*, 264−269.

(34) Zhang, T.; Fujisawa, K.; Zhang, F.; Liu, M.; Lucking, M. C.; Gontijo, R. N.; Lei, Y.; Liu, H.; Crust, K.; Granzier-Nakajima, T.; Terrones, H.; Elías, A. L.; Terrones, M. Universal *In Situ* Substitutional Doping of Transition Metal Dichalcogenides by Liquid-Phase Precursor-Assisted Synthesis. *ACS Nano* **2020**, *14*, 4326−4335.

(35) Duan, X.; Wang, C.; Shaw, J. C.; Cheng, R.; Chen, Y.; Li, H.; Wu, X.; Tang, Y.; Zhang, Q.; Pan, A.; Jiang, J.; Yu, R.; Huang, Y.; Duan, X. Lateral Epitaxial Growth of Two-Dimensional Layered Semiconductor Heterojunctions. *Nat. Nanotechnol.* **2014**, *9*, 1024−1030.

(36) Yang, J.; Mohmad, A. R.; Wang, Y.; Fullon, R.; Song, X.; Zhao, F.; Bozkurt, I.; Augustin, M.; Santos, E. J. G.; Shin, H. S.; Zhang, W.; Voiry, D.; Jeong, H. Y.; Chhowalla, M. Ultrahigh-Current-Density Niobium Disulfide Catalysts for Hydrogen Evolution. *Nat. Mater.* **2019**, *18*, 1309−1314.

(37) Zhou, J.; Tang, B.; Lin, J.; Lv, D.; Shi, J.; Sun, L.; Zeng, Q.; Niu, L.; Liu, F.; Wang, X.; Liu, X.; Suenaga, K.; Jin, C.; Liu, Z. Morphology Engineering in Monolayer MoS_2-WS_2 Lateral Heterostructures. *Adv. Funct. Mater.* **2018**, *28*, 1801568.

(38) Liang, L.; Meunier, V. First-Principles Raman Spectra of MoS_2, WS_2 and Their Heterostructures. *Nanoscale* **2014**, *6*, 5394−5401.

(39) Hong, X.; Kim, J.; Shi, S.-F.; Zhang, Y.; Jin, C.; Sun, Y.; Tongay, S.; Wu, J.; Zhang, Y.; Wang, F. Ultrafast Charge Transfer in Atomically Thin MoS_2/WS_2 Heterostructures. *Nat. Nanotechnol.* **2014**, *9*, 682−686.

(40) Zheng, S.; Sun, L.; Yin, T.; Dubrovkin, A. M.; Liu, F.; Liu, Z.; Shen, Z. X.; Fan, H. J. Monolayers of $W_xMo_{1-x}S_2$ Alloy Heterostructure with In-Plane Composition Variations. *Appl. Phys. Lett.* **2015**, *106*, 063113.

(41) Chen, Y.; Xi, J.; Dumcenco, D. O.; Liu, Z.; Suenaga, K.; Wang, D.; Shuai, Z.; Huang, Y.-S.; Xie, L. Tunable Band Gap Photoluminescence from Atomically Thin Transition-Metal Dichalcogenide Alloys. *ACS Nano* **2013**, *7*, 4610−4616.

(42) Gurarslan, A.; Yu, Y.; Su, L.; Yu, Y.; Suarez, F.; Yao, S.; Zhu, Y.; Ozturk, M.; Zhang, Y.; Cao, L. Surface-Energy-Assisted Perfect Transfer of Centimeter-Scale Monolayer and Few-Layer MoS_2 Films onto Arbitrary Substrates. *ACS Nano* **2014**, *8*, 11522−11528.

(43) Cain, J. D.; Shi, F.; Wu, J.; Dravid, V. P. Growth Mechanism of Transition Metal Dichalcogenide Monolayers: The Role of Self-Seeding Fullerene Nuclei. *ACS Nano* **2016**, *10*, 5440−5445.

(44) Li, Y.; Hao, S.; DiStefano, J. G.; Murthy, A. A.; Hanson, E. D.; Xu, Y.; Wolverton, C.; Chen, X.; Dravid, V. P. Site-Specific Positioning and Patterning of MoS_2 Monolayers: The Role of Au Seeding. *ACS Nano* **2018**, *12*, 8970−8976.

(45) Shi, J.; Ma, D.; Han, G.-F.; Zhang, Y.; Ji, Q.; Gao, T.; Sun, J.; Song, X.; Li, C.; Zhang, Y.; Lang, X.-Y.; Zhang, Y.; Liu, Z. Controllable Growth and Transfer of Monolayer MoS_2 on Au Foils and Its Potential Application in Hydrogen Evolution Reaction. *ACS Nano* **2014**, *8*, 10196−10204.

(46) An, Y.-R.; Fan, X.-L.; Luo, Z.-F.; Lau, W.-M. Nanopolygons of Monolayer MS_2: Best Morphology and Size for HER Catalysis. *Nano Lett.* **2017**, *17*, 368−376.

(47) Mun, J.; Park, H.; Park, J.; Joung, D.; Lee, S.-K.; Leem, J.; Myoung, J.-M.; Park, J.; Jeong, S.-H.; Chegal, W.; Nam, S.; Kang, S.-W. High-Mobility MoS_2 Directly Grown on Polymer Substrate with Kinetics-Controlled Metal-Organic Chemical Vapor Deposition. *ACS Appl. Electron. Mater.* **2019**, *1*, 608−616.

(48) Lu, J.; Yeo, P. S. E.; Gan, C. K.; Wu, P.; Loh, K. P. Transforming C_{60} Molecules into Graphene Quantum Dots. *Nat. Nanotechnol.* **2011**, *6*, 247−252.

(49) Coraux, J.; N'Diaye, A. T.; Engler, M.; Busse, C.; Wall, D.; Buckanie, N.; Meyer zu Heringdorf, F.-J; van Gastel, R.; Poelsema, B.; Michely, T. Growth of Graphene on Ir(111). *New J. Phys.* **2009**, *11*, 023006.

(50) Wang, Q.; Li, N.; Tang, J.; Zhu, J.; Zhang, Q.; Jia, Q.; Lu, Y.; Wei, Z.; Yu, H.; Zhao, Y.; Guo, Y.; Gu, L.; Sun, G.; Yang, W.; Yang, R.; Shi, D.; Zhang, G. Wafer-Scale Highly Oriented Monolayer MoS_2 with Large Domain Sizes. *Nano Lett.* **2020**, *20*, 7193−7199.

(51) Li, N.; Wang, Q.; Shen, C.; Wei, Z.; Yu, H.; Zhao, J.; Lu, X.; Wang, G.; He, C.; Xie, L.; Zhu, J.; Du, L.; Yang, R.; Shi, D.; Zhang, G. Large-Scale Flexible and Transparent Electronics Based on Monolayer Molybdenum Disulfide Field-Effect Transistors. *Nat. Electron.* **2020**, *3*, 711−717.

(52) Choi, C.; Choi, M. K.; Liu, S.; Kim, M. S.; Park, O. K.; Im, C.; Kim, J.; Qin, X.; Lee, G. J.; Cho, K. W.; Kim, M.; Joh, E.; Lee, J.; Son, D.; Kwon, S.-H.; Jeon, N. L.; Song, Y. M.; Lu, N.; Kim, D.-H. Human Eye-Inspired Soft Optoelectronic Device Using High-Density MoS_2-Graphene Curved Image Sensor Array. *Nat. Commun.* **2017**, *8*, 1664.

(53) Choi, C.; Leem, J.; Kim, M. S.; Taqieddin, A.; Cho, C.; Cho, K. W.; Lee, G. J.; Seung, H.; Bae, H. J.; Song, Y. M.; Hyeon, T.; Aluru, N. R.; Nam, S.; Kim, D.-H. Curved Neuromorphic Image Sensor Array Using a MoS_2-Organic Heterostructure Inspired by The Human Visual Recognition System. *Nat. Commun.* **2020**, *11*, 5934.

(54) Di Bartolomeo, A.; Genovese, L.; Foller, T.; Giubileo, F.; Luongo, G.; Croin, L.; Liang, S.-J.; Ang, L K; Schleberger, M. Electrical Transport and Persistent Photoconductivity in Monolayer MoS_2 Phototransistors. *Nanotechnology* **2017**, *28*, 214002.